Diamond & Related Materials 170 (2026) 114327

Contents lists available at ScienceDirect

Diamond & Related Materials

journal homepage: www.elsevier.com/locate/diamond

Dual-pathway valorization of black liquor lignin into activated and hard carbons with complementary structure–property relationships for sustainable supercapacitor applications

Anit Joseph [a], Varna N. Preman [a], Tiju Thomas [a,b,*]

[a] Department of Metallurgical and Materials Engineering, Indian Institute of Technology Madras, Chennai, 600036, India
[b] Center for Resource Efficiency, Recyclability and Circularity in Energy Transition, School of Sustainability, Indian Institute of Technology Madras, Chennai, 600036, India

ARTICLE INFO

Keywords:
Black liquor
Lignin valorization
Hard carbon
Biomass-derived carbon
Aqueous supercapacitors

ABSTRACT

The increasing demand for sustainable carbon materials has intensified interest in valorizing lignin-rich industrial by-products for energy storage applications. Black liquor, a major by-product of the pulp and paper industry, represents an abundant yet underutilized lignin resource with significant environmental implications if inadequately managed. In this work, black-liquor-derived lignin was converted into two structurally distinct carbon materials through complementary synthesis routes: hierarchically porous activated carbon (AC) via chemical activation and dense hard carbon (HC) via controlled pyrolysis. The dual-pathway strategy enabled systematic tailoring of pore architecture, surface chemistry, and carbon microstructure, resulting in distinct electrochemical characteristics. Structural and physicochemical analyses revealed that chemical activation generated a highly porous carbon with a specific surface area of 1503 $m^2 g^{-1}$, whereas pyrolysis produced a compact hard carbon with limited porosity but a more continuous carbon framework. Electrochemical evaluation in 3 M KOH demonstrated that AC exhibited a higher specific capacitance of 191 F/g owing to its well-developed microporous structure, while HC delivered superior rate capability, higher coulombic efficiency (~93%), reduced self-discharge, and enhanced cycling stability (90% capacitance retention after 5000 cycles), attributed to its dense architecture and efficient electron transport pathways. Furthermore, the asymmetric AC//HC device effectively integrated the complementary characteristics of both carbons, providing balanced energy and power performance. This study demonstrates an effective strategy for converting black liquor into value-added functional carbon materials and highlights the potential of dual-pathway lignin valorization to develop sustainable electrode materials for aqueous supercapacitors.

1. Introduction

The transition toward sustainable energy storage systems requires replacing petroleum-derived carbons with renewable, environmentally benign alternatives. In this context, biomass-derived carbons have emerged as promising candidates due to their low cost, abundance, and tunable physicochemical properties [1]. Among various biomass resources, lignin stands out as the second most abundant natural polymer after cellulose, accounting for a significant fraction of lignocellulosic biomass and industrial waste streams [2,3]. Despite its availability, the majority of lignin generated in the pulp and biorefinery industries is underutilized, often incinerated for low-value energy recovery, resulting in substantial carbon emissions and resource waste [4]. Therefore, valorizing lignin into high-value functional carbon materials represents a critical step toward circular carbon economies.

Black liquor, a major by-product of the kraft pulping process, is particularly rich in lignin and is a dominant source of industrial wastewater pollution, accounting for nearly 90% of the total pollutant load in the paper industry [5]. Conventionally, black liquor is either discharged or combusted, posing severe environmental challenges. However, its intrinsic composition, comprising lignin, inorganic salts, and residual organics, offers a unique opportunity for direct conversion into advanced carbon materials. Recent studies have demonstrated that black-liquor-derived carbons can exhibit high surface areas (>2000 $m^2 g^{-1}$) and tunable hierarchical porosity, enabling enhanced ion transport and charge storage for supercapacitor applications [6,7]. Nevertheless,

* Corresponding author at: Department of Metallurgical and Materials Engineering, Indian Institute of Technology Madras, Chennai, 600036, India.
E-mail addresses: tijuthomas@smail.iitm.ac.in, tijuthomas@iitm.ac.in (T. Thomas).

https://doi.org/10.1016/j.diamond.2026.114327
Received 11 August 2026; Received in revised form 13 October 2026; Accepted 22 October 2026
Available online 26 October 2026
0925-9635/© 2026 Elsevier B.V. All rights are reserved, including those for text and data mining, AI training, and similar technologies.

rational control over structure–property relationships in such systems remains a key challenge.

Lignin is inherently well-suited as a carbon precursor due to its aromatic three-dimensional polymeric backbone, high carbon content, and abundance of oxygen-containing functional groups. These features facilitate high carbon yield during pyrolysis and enable the formation of stable graphitic domains with tunable porosity. Moreover, the presence of intrinsic heteroatoms (O and potentially S from pulping processes) provides opportunities for in situ heteroatom doping, which can further enhance surface wettability, pseudocapacitance, and electronic conductivity [3,5]. Such structural advantages make lignin-derived carbons highly attractive for electrochemical energy storage, particularly in aqueous supercapacitors where rapid ion transport and surface accessibility are critical.

Carbon materials remain the cornerstone of electrochemical supercapacitors due to their chemical stability (stable operation over $>10^5$ charge–discharge cycles in aqueous electrolytes), electrical conductivity (typically 10^5–10^0 S/cm, depending on graphitization), and structural tunability [8]. Among them, activated carbon (AC) and hard carbon (HC) represent fundamentally distinct architectures with contrasting charge-storage behaviors. AC typically exhibits a highly developed microporous structure and large specific surface area, enabling efficient electric double-layer formation and high specific capacitance. However, excessive microporosity can restrict ion transport at high current densities, limiting rate capability and power performance [5,9].

Although lignin-derived carbons have gained significant attention, several critical gaps remain. First, black-liquor-derived lignin is still underutilized despite being an abundant industrial waste stream with high carbon content and inherent inorganic species that can promote pore formation. Second, existing studies predominantly focus on producing single-phase porous carbons, with very limited reports demonstrating the synthesis of dual carbon systems (AC and HC) from the same lignin precursor. This work directly contributes to multiple United Nations Sustainable Development Goals (SDGs) by integrating waste valorization with energy storage. The conversion of pulp-mill black liquor, responsible for a major fraction of the pollutant load in kraft pulping effluents [5], into functional carbon materials aligns with SDG 12 (Responsible Consumption and Production) by promoting circular resource utilization. By mitigating the discharge of this high-organic-load effluent, the approach also supports SDG 6 (Clean Water and Sanitation) by reducing water pollution [10]. Furthermore, the development of high-performance electrode materials for aqueous supercapacitors advances SDG 7 (Affordable and Clean Energy). Finally, the scalable transformation of an industrial by-product into value-added materials underscores SDG 9 (Industry, Innovation and Infrastructure), fostering sustainable industrial practices.

To substantiate the relevance to sustainability, a back-of-the-envelope assessment highlights the scale of the impact. The pulp and paper industry generates ~7 t of black liquor per tonne of pulp, corresponding to an estimated 0 million tonnes annually in India alone [11]. Given that black liquor contains ~35–45% lignin [12], this represents a substantial and underutilized carbon-rich resource. Conventional practice involves incineration in recovery boilers, leading to immediate CO_2 emissions [13,14]. In contrast, the present approach converts lignin into functional carbon materials with practical yields of ~10–20 wt% for activated carbon and ~ 30–40 wt% for hard carbon [15,16]. Considering that lignin contains ~60% carbon, diverting even a fraction of this stream into electrode materials can avoid on the order of ~1–2 t of CO_2 equivalent per tonne of lignin processed. These estimates underscore the potential of black liquor valorization not only for sustainable materials production but also for meaningful carbon mitigation at scale.

This work proposes a unified and scalable strategy to convert black-liquor-derived lignin into two structurally distinct carbons: activated carbon (AC) and hard carbon (HC). By deriving both materials from the same precursor, this study eliminates variability associated with feedstock differences and enables a direct comparison of porous and dense carbon architectures. The intrinsic charge storage behavior of AC and HC is systematically investigated using three-electrode measurements, followed by evaluation in practical two-electrode configurations, including symmetric (AC//AC and HC//HC) and asymmetric (AC//HC) devices.

By bridging waste valorization and rational carbon design, this study provides new insights into the engineering of functionally complementary carbon materials for high-performance and sustainable aqueous supercapacitors.

2. Experimental section

2.1. Materials used

The black liquor was collected from Kerala Paper Products Limited (KPPL) in Kerala, India. For electrode slurry preparation, polyvinylidene fluoride (PVDF, Thermoscientific) was used as the binder, and *N*-methyl-2-pyrrolidone (NMP, SRL, 99.5%) was used as the solvent. The electrolyte was prepared from potassium hydroxide (KOH, Qualigens, 85%). Carbon paper used as a current collector was purchased from The Electrode Store (TES). Acetone and hydrochloric acid (HCl, 35–37% assay) were used for cleaning the substrate. Deionized water was used for washing purposes.

2.2. Synthesis of AC and HC

2.2.1. Extraction of lignin from black liquor

Lignin was extracted from black liquor via acid precipitation. Briefly, 1 M HCl was added dropwise to the black liquor under continuous stirring until the pH reached 2–3, resulting in lignin precipitation. The suspension was further stirred continuously for 6–12 h to ensure complete precipitation. The precipitated lignin was separated and thoroughly washed with deionized (DI) water until the pH was neutral. The obtained slurry was then dried in a vacuum oven at 80 °C overnight to yield purified lignin powder. The yield of lignin was approximately 2.3 g per 100 mL of black liquor.

2.2.2. Synthesis of activated carbon (AC)

The extracted lignin was first pre-carbonized under a nitrogen atmosphere at 600 °C for 1 h (heating rate ~ 5 °C min^{-1}) to obtain an intermediate carbon product. For activation, the obtained carbon was mixed with KOH at a 1:4 (carbon: KOH) weight ratio using a 10 wt% KOH solution. The mixture was stirred continuously for 12 h to ensure uniform impregnation. Subsequently, the mixture was transferred to a Teflon-lined autoclave and subjected to a hydrothermal treatment at 200 °C for 6 h. The sample is then dried and pyrolyzed at 800 °C for 1.5 h. After the reaction, the product was washed with dilute HCl and then DI water until a neutral pH was reached, to remove residual inorganic species. The final product was dried at 80 °C overnight to obtain activated carbon (AC). The yield of activated carbon (AC) is 26.8% (Fig. 1).

2.2.3. Synthesis of hard carbon (HC)

Hard carbon was synthesized via direct pyrolysis of lignin. Approximately 2.5 g of lignin powder was subjected to high-temperature treatment under a nitrogen atmosphere at 1200 °C for 2 h to obtain a lignin-derived hard carbon (Fig. 1). The yield of hard carbon (HC) is 40%.

2.3. Characterization techniques

The amorphous nature of activated carbon was confirmed using X-ray diffraction (XRD) on a Rigaku and a Miniflex 6G benchtop diffractometer. The morphological details were analyzed using a field-emission scanning electron microscope (FESEM) (Apreo, operating at voltages ranging from −200 V to 30 kV). The elements were confirmed using energy-dispersive X-ray spectroscopy (EDAX) and X-ray photoelectron

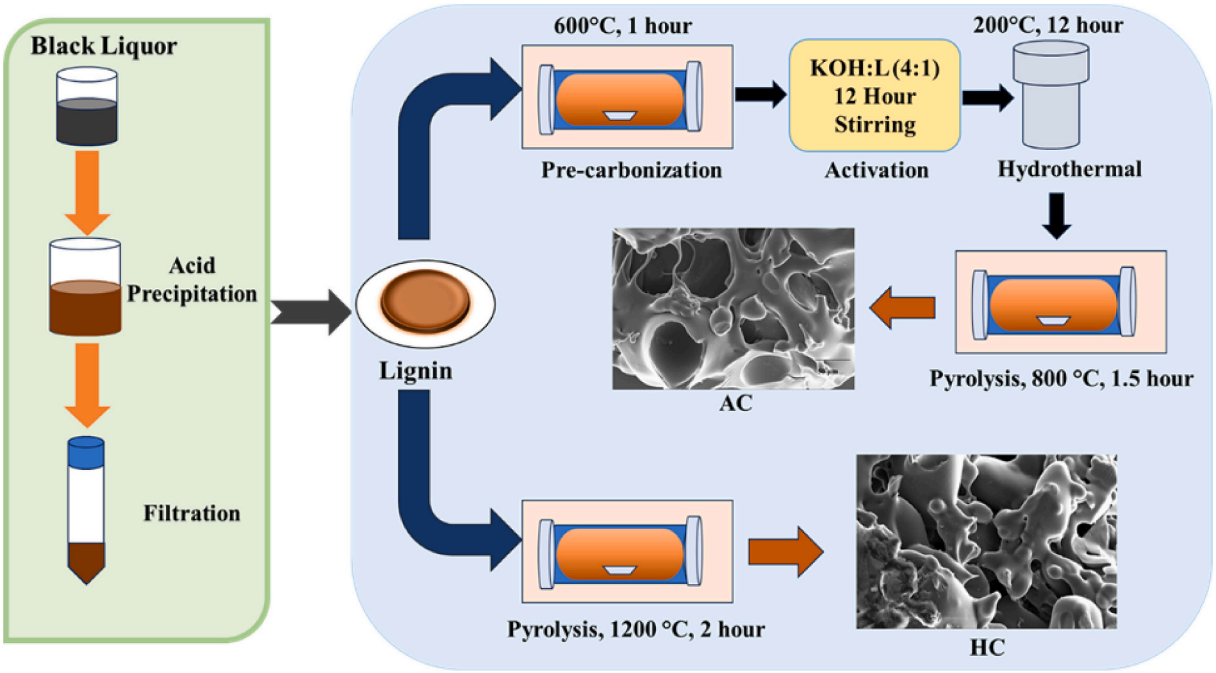

Fig. 1. Schematic illustration of the AC and HC synthesis procedure.

spectroscopy (XPS, X-ray Source: Al K-alpha). The structure and properties of carbon were confirmed using Raman spectroscopy (Confocal Raman Microscope-Alpha300 S). Brunauer-Emmett-Teller (BET) experiments were performed using a Micromeritics ASAP 2020 porosimeter. Electrical sheet resistance was measured using a Signatone Pro-4 four-point collinear probe setup coupled with a Keithley 2450 Source meter unit. The surface wettability of the carbon samples was evaluated by contact angle measurements using an Apex ACAM D3 goniometer. Thermogravimetric analysis (TGA) and differential scanning calorimetry (DSC) were performed using a SETARAM SETLINE thermal analysis system to investigate the thermal stability and thermal transitions of the samples.

2.4. Electrochemical studies

The carbon paper current collector was cleaned using a standard cleaning procedure [17]. Electrochemical measurements were performed using a CHI 7081C electrochemical workstation in a standard three-electrode configuration. The working electrode was prepared by mixing 95 wt% activated carbon and 5 wt% PVDF in NMP to form a slurry, which was then brush-coated onto a 1 cm × 1 cm carbon paper and dried at 80 °C overnight. The electrolyte was prepared using 3 M potassium hydroxide. A Pt foil (1 × 2 cm^2) was used as the counter electrode, and an Ag/AgCl electrode serves as the reference. The same electrochemical measurements were also performed using a 2-E setup (Swagelok) for both symmetric and asymmetric devices.

3. Result and discussion

A Bruker powder XRD device is used to examine the diffraction pattern of synthesized lignin, activated carbon, and hard carbon. The diffraction pattern is used to determine the crystallite size and phase purity. The XRD plot of lignin in Fig. 2a revealed a large peak in the region $2\theta \approx 22°$, suggesting its extremely amorphous nature [18]. Similar XRD patterns are observed in lignin-derived carbons such as AC and HC; these samples exhibit two broad reflection peaks at 22–23° and 42–44°, respectively, which are attributed to the (002) and (100) crystallographic planes in the disordered carbon structure [19]. More specifically, all these peaks are broad, suggesting that the samples' amorphous nature match those of both AC and HC [6,20]. The d-spacing between the (002) plane of AC and HC is 0.40 nm and 0.38 nm, respectively, calculated by Bragg's law. It is clear that structural evolution from amorphous lignin to turbostratic activated and hard carbons. While lignin shows no crystalline order, activated carbon exhibits highly disordered carbon layers with expanded interlayer spacing. In contrast, hard carbon shows relatively improved graphene-layer stacking, indicating higher structural ordering.

One common nondestructive method for characterizing crystalline, nanocrystalline, and amorphous carbons is Raman spectroscopy. Raman spectra (Fig. 2b) of lignin-derived activated carbon and hard carbon exhibit characteristic D (~1350 cm^{-1}) and G (~1580 cm^{-1}) bands, confirming the presence of sp^2-hybridized carbon structures and sp^2 C—C vibrations in planar graphite, respectively [21–23]. The G and D peaks of the Raman spectra of nanocrystalline and amorphous carbons, even those without extensive graphitic ordering, are nonetheless dominated by variable intensity, position, and width. The HC sample shows sharper, better-defined D and G bands than the AC sample, indicating a higher degree of structural ordering. Quantitatively, AC exhibits a higher I_D/I_G ratio (~1.6), suggesting a greater degree of structural disorder, whereas HC shows a lower I_D/I_G ratio (~0.81), indicative of reduced defects and relatively larger graphitic domains [8]. This observation is consistent with the XRD results.

The surface chemical composition and electronic structure of the samples are analyzed using X-ray photoelectron spectroscopy (XPS), as shown in Fig. 2c and d. The high-resolution C 1s spectra of both activated carbon (AC) and hard carbon (HC) exhibit a dominant peak at ~284.5 eV, corresponding to sp^2-hybridized C–C/C=C bonds. The significantly higher intensity of this peak in AC indicates greater graphitization. In contrast, HC shows reduced graphitic carbon intensity, along with pronounced features at higher binding energies (~291–295 eV), attributed to oxygen-containing functional groups such as C—O, C═O, and O–C=O, suggesting increased surface functionalization and defect density.

The O 1s spectra further support this observation: HC shows a stronger, broader peak centered at ~530–532 eV, indicating a higher concentration of oxygen functionalities (e.g., hydroxyl, carbonyl, and

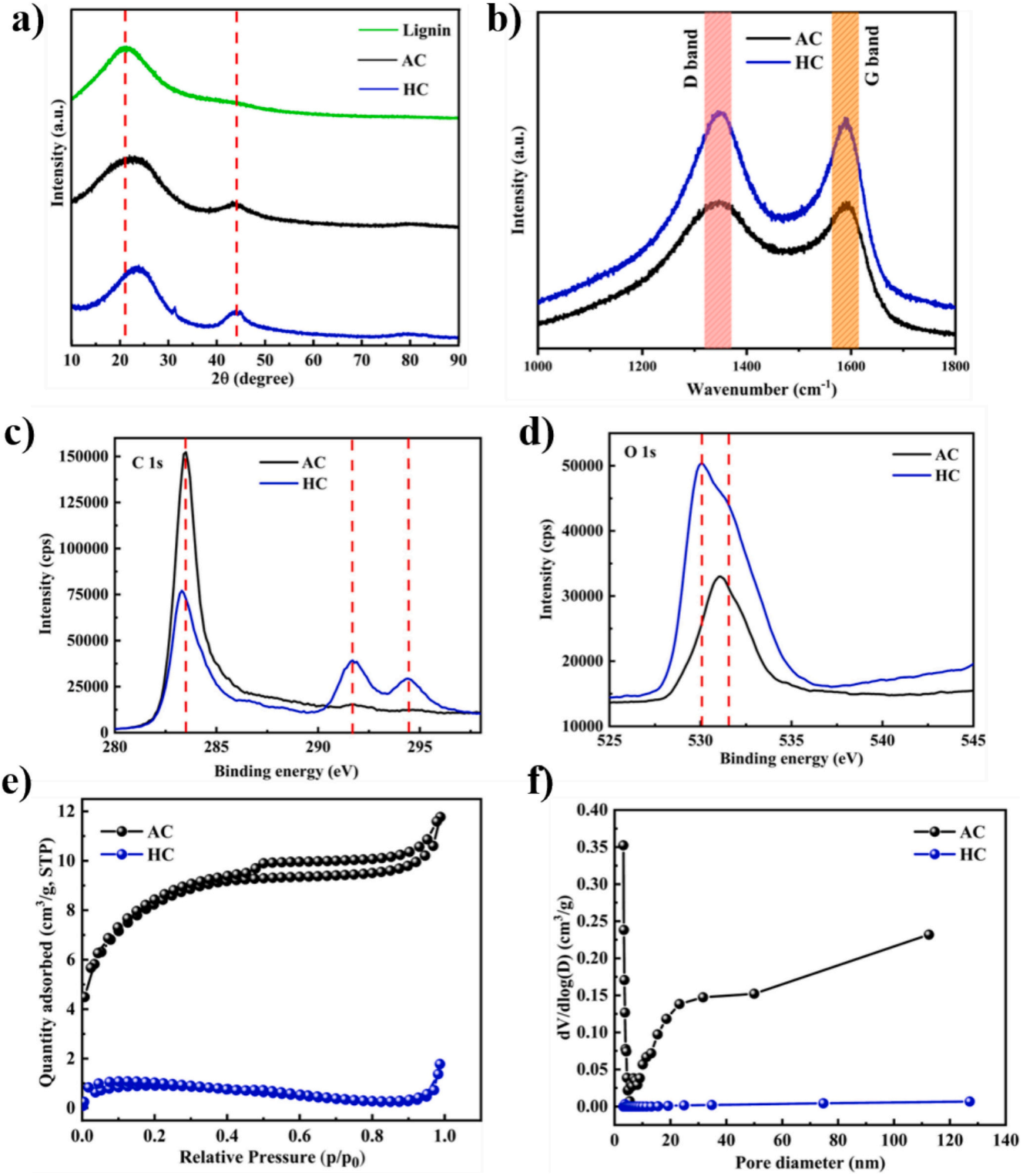

Fig. 2. a) Powder X-ray diffraction (XRD) patterns of lignin (green), activated carbon (AC, black), and hard carbon (HC, blue), b) Raman spectra of activated carbon (AC) and hard carbon (HC), High-resolution XPS spectra of c) C 1s and d) O 1s regions for activated carbon (AC) and hard carbon (HC), e) Nitrogen adsorption–desorption isotherms f) pore size distributions of activated carbon (AC) and hard carbon (HC).

carboxyl groups), whereas AC exhibits a relatively weaker signal, consistent with its more ordered carbon framework. The higher oxygen content observed for HC by XPS is expected to influence its charge-storage mechanism through both enhanced electrolyte accessibility and surface redox activity. Polar oxygen-containing functionalities improve the hydrophilicity of the carbon surface, facilitating electrolyte wetting and ion penetration into accessible pores and thereby enhancing the electric double-layer capacitance. In addition, electrochemically active oxygen functionalities, particularly carbonyl- and quinone-type groups, can undergo reversible surface redox reactions, thereby contributing additional pseudocapacitance. Thus, the oxygen-rich surface of HC can provide a combined EDLC–pseudocapacitive contribution

to charge storage. However, the XPS data alone cannot quantitatively separate these two contributions. Overall, AC is characterized by a highly graphitized structure with limited surface functionalities, whereas HC is enriched with oxygen-containing groups that can provide additional active sites and enhance electrochemical reactivity. The XPS spectra exhibit characteristic features of lignin-derived carbons, with binding energies and functional group distributions in close agreement with previously reported studies, thereby validating the structural and chemical composition of the synthesized materials [24–26].

XPS peak deconvolution (Fig.S1) reveals distinct surface chemical environments in activated carbon (AC) and hard carbon (HC). In the C 1s spectrum, AC (Fig.S1a) exhibits three components (45.2%, 30.8%, and 24.0%), whereas HC (Fig.S1b) displays four components (34.5%, 28.8%, 20.8%, and 15.9%), indicating a broader distribution of carbon bonding environments in HC. The O 1s spectra also show contrasting component distributions, with contributions of 94.3% and 5.7% for AC (Fig.S1c) and 29.9% and 70.1% for HC (Fig. S1d).

The nitrogen adsorption–desorption isotherms and corresponding pore-size distributions of activated carbon (AC) and hard carbon (HC) are presented in Fig. 2e and f, respectively. AC exhibits substantially higher nitrogen uptake, particularly at low relative pressures ($P/P_o < 0.1$), indicating greater micropore accessibility and a considerably larger specific surface area. The hysteresis observed at intermediate-to-high relative pressures suggests the presence of mesopores in AC. In contrast, HC exhibits very limited nitrogen adsorption, consistent with its much lower Brunauer–Emmett–Teller (BET) specific surface area of 5 $m^2\ g^{-1}$ compared with 1503 $m^2\ g^{-1}$ for AC [24,27].

The pronounced difference in surface area reflects the contrasting carbon structures produced by the two synthesis routes. Chemical activation promotes extensive pore development in AC, whereas direct high-temperature pyrolysis without activation produces a comparatively dense carbon structure with limited nitrogen-accessible porosity. Although the pore-size distribution of HC extends over a broader size range, its extremely low BET surface area indicates that the overall contribution of accessible pores is limited. Furthermore, nitrogen adsorption at 77 K may not fully characterize closed pores or pores that are inaccessible to nitrogen under the measurement conditions.

These results establish AC as a highly porous, surface-area-dominated carbon, whereas HC exhibits a comparatively dense structure with limited nitrogen-accessible porosity. The developed porosity of AC provides abundant accessible surface sites for electrochemical charge storage. In contrast, the potential contribution of HC to ion transport and charge storage should be interpreted in conjunction with its electrochemical performance rather than attributed solely to its pore-size distribution.

FESEM images (Fig. 3) and corresponding EDS analysis of (a-c) activated carbon (AC) and (d-f) hard carbon (HC). The SEM images reveal a highly porous structure in AC, with well-developed, interconnected pores, while HC exhibits a relatively denser morphology with partially collapsed, irregular pores. The EDS spectra confirm the predominant presence of carbon, along with oxygen and trace potassium. Quantitative analysis shows higher carbon content in AC (93.1%), whereas HC contains relatively increased oxygen (15.1%). These observations highlight the structural and compositional differences between AC and HC. To confirm the purity, morphology, and elemental composition of the extracted lignin, SEM and EDS analysis were performed (Fig. S2a, b). The results confirm that the extracted material predominantly consists of carbon and oxygen, with no significant inorganic impurities detected.

The thermal behavior of the lignin-derived activated carbon (AC) and hard carbon (HC) was investigated using thermogravimetric analysis (TGA) coupled with differential scanning calorimetry (DSC) under a nitrogen atmosphere up to 800 °C and 650 °C, respectively (Fig. S3a, b). Both samples exhibit multistage mass loss, indicating the release of residual volatile species and the thermal decomposition of labile surface functionalities. As the samples were already carbonized, the observed weight loss primarily reflects the thermal response of the existing carbon materials rather than the initial conversion of lignin into carbon.

At lower temperatures, the initial mass loss is primarily due to the desorption of physically adsorbed moisture and other weakly retained volatile species. The more pronounced low-temperature mass-loss feature observed for AC suggests a distinct contribution from desorption or the release of thermally labile species. In the intermediate-temperature region, further mass loss may arise from the decomposition of residual oxygen-containing surface groups, including carboxyl, hydroxyl, carbonyl, and ether-related functionalities. At higher temperatures, the continued mass loss may be associated with the removal of more thermally stable surface functionalities and residual volatile species, together with further structural rearrangement of the carbonaceous matrix.

The TGA curves show that HC undergoes more pronounced initial weight loss below approximately 150 °C, whereas AC exhibits a sharp initial mass-loss step near 50–70 °C, followed by a relatively stable region. Above approximately 150 °C, both materials exhibit similar gradual mass loss, reaching a residual mass of approximately 75% at 800 °C. In the DSC profiles, AC displays a pronounced thermal event near 60–70 °C, while HC exhibits a broader feature around 50–100 °C and additional thermal events at approximately 150–200 °C. At higher

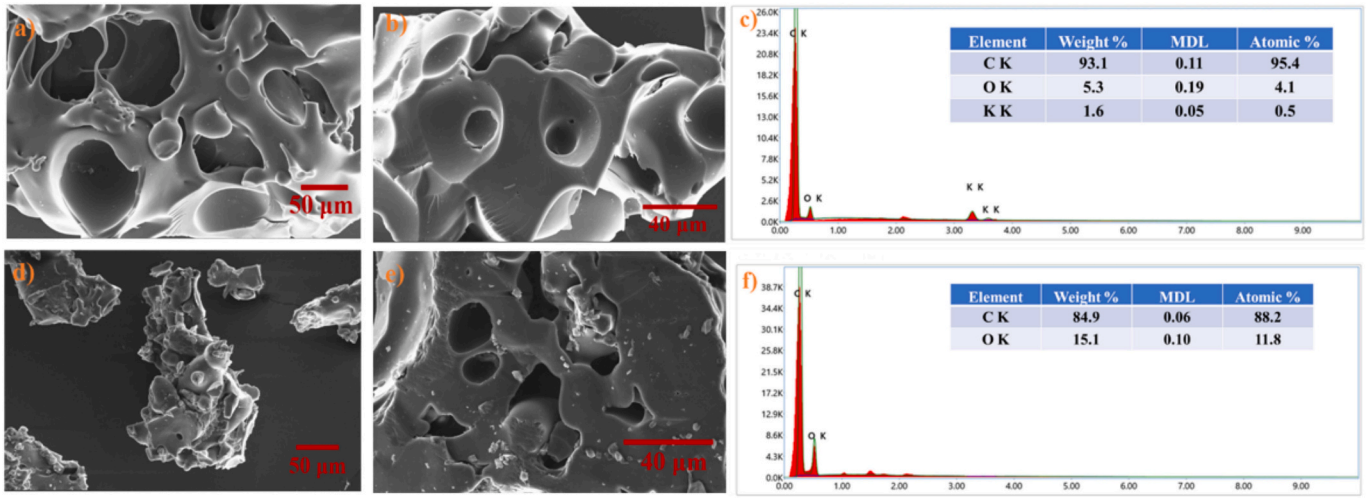

Fig. 3. FESEM images of a, b) activated carbon (AC) and d, e) hard carbon (HC), and c,f) corresponding EDS spectra and elemental composition. AC exhibits a highly porous, interconnected network, whereas HC shows a relatively denser structure with irregular and partially collapsed pores.

temperatures, HC shows a continuous downward heat-flow trend, whereas AC exhibits a relatively broad feature around 400–500 °C, followed by a sharp decline above 550 °C. These differences suggest distinct residual surface chemistries and thermal decomposition behaviors in AC and HC.

The KOH electrolyte contact angle measurements show values of 100.3° for activated carbon (AC, Fig. S4a) and 108.9° for hard carbon (HC, Fig. S4b). Both electrodes exhibit contact angles greater than 90°, indicating relatively poor wettability by the KOH electrolyte, with HC showing lower wettability than AC. The comparatively lower contact angle of AC suggests more favorable electrolyte–electrode interfacial contact, potentially supporting electrolyte access to its hierarchical porous structure. In contrast, the higher contact angle of HC indicates a less wettable surface, which may be associated with differences in surface roughness, pore structure, surface heterogeneity, sample compaction, and measurement protocol. These differences in wettability may influence electrolyte penetration and ion accessibility during supercapacitor operation. However, contact angle measurements alone cannot establish electrolyte infiltration into internal pores; this also depends on pore architecture and electrode structure.

Four-point-probe measurements were performed to evaluate the electrical properties of the activated carbon (AC) and hard carbon (HC).

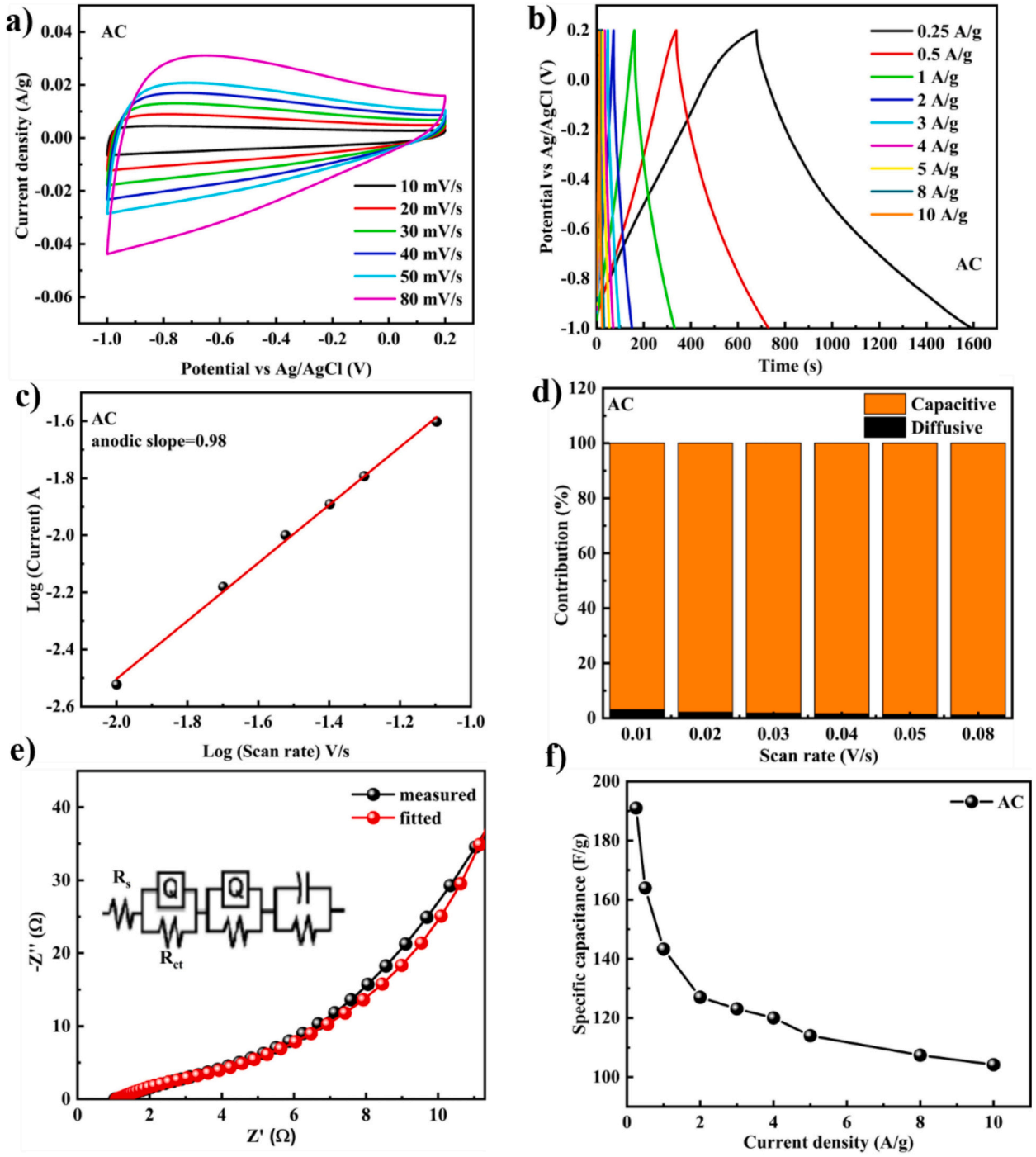

Fig. 4. 3-electrode measurements of lignin derived AC a) CV at varying scan rate in 3 M KOH electrolyte, b) GCD at varying current density, c) power-law analysis of peak current vs scan rate, d) quantitative separation of charge storage contributions at different scan rates, e) Nyquist plot obtained using EIS analysis and equivalent circuit is shown in the inset, and f) specific capacitance vs. current density plot.

The AC and HC samples exhibited sheet resistances of 60.37 and 10.79 kΩ/sq., corresponding to electrical conductivities of 0.414 and 1.323 S/m, respectively. The HC coating, therefore, exhibited approximately 3.2 times higher electrical conductivity than the AC coating, indicating improved electrical transport within the prepared HC layer. The conductivity of AC is in close agreement with the value of 0.41 S/m reported for KOH-activated carbon derived from empty oil palm fruit bunches using a four-point probe method [28]. Furthermore, Hoffmann et al. reported an electrical conductivity of 0.08 S/m for biochar carbonized at 600 °C, which increased substantially following KOH activation [28]. Although the latter material is not identical to the present hard carbon, it provides a useful comparison with relatively low-conductivity biomass-derived carbon. The higher conductivity of HC than AC in the present study may be attributed to differences in carbon structure, particle-to-particle contact, and coating morphology. These values should be interpreted as effective conductivities of the prepared coatings, particularly because porosity, coating uniformity, and substrate contributions can influence four-point-probe measurements.

3.1. Electrochemical studies

3.1.1. 3-Electrode measurements

The electrochemical performance of the synthesized activated carbon (AC) and hard carbon (HC) electrodes is evaluated using a three-electrode configuration. The working electrodes are prepared by coating the active material onto carbon paper substrates, while a platinum (Pt) foil and an Ag/AgCl electrode are employed as the counter and reference electrodes, respectively. All measurements are carried out in an aqueous 3 M KOH electrolyte. The active mass loadings of the AC and HC electrodes in 3-electrode measurements are 2.64 and 2.72 mg, respectively.

This configuration enables accurate assessment of the intrinsic electrochemical behavior of electrode materials, including their capacitive characteristics, charge-storage mechanisms, and ion-transport properties, without interference from full-cell limitations.

The cyclic voltammograms (CVs) of lignin-derived AC at various scan rates (10–80 mV/s) (Fig. 4a) exhibit quasi-rectangular shapes with slight distortion at higher scan rates. The CV shows a stable potential window of 0.2 V to −1.0 V vs Ag/AgCl. The CV shape suggests that electrical double-layer capacitance (EDLC) is primarily responsible for charge storage. This behavior is consistent with the traditional EDLC process described in [28], which yields rectangular CV profiles devoid of redox peaks due to electrostatic adsorption of ions at the electrode-electrolyte interface. The absence of redox peaks confirms non-faradaic charge storage typical of activated carbon materials, as reported by Zhang et al. [29].

The GCD profiles at different current densities (0.25–10 A/g) (Fig. 4b) display nearly symmetric triangular shapes, confirming highly reversible capacitive behavior. The linear charge-discharge curves indicate good coulombic efficiency and low polarization. At lower current densities (0.25 A/g), longer discharge times are observed, corresponding to higher specific capacitance. As the current density increases, the discharge time decreases due to limited ion diffusion at high rates, a phenomenon typical of porous carbon electrodes. The specific capacitance is calculated from the GCD curve using Eq. (1)

$$C_{sp} = \frac{I \times t_d}{m \times \Delta V} \tag{1}$$

where m is the active mass loading on the current collector (carbon paper) in mg, t_d is the discharge period in seconds (s), and ΔV is the potential window in volts, $\frac{I}{m}$ is the current density in A/g, and C_{sp} is the specific capacitance in F/g. The specific capacitance is calculated as 191 F/g at a current density of 0.25 A/g.

According to Sevilla M et al. [30] microporous biomass-derived carbons exhibit high capacitance at low rates but limited performance at high current densities due to diffusion limitations. This behavior is consistent with their findings. A small IR drop is observed at the beginning of discharge, indicating relatively low internal resistance and good electrical conductivity of the electrode. Such behavior is typical of well-activated carbon materials and is supported by previous reports, which show that minimal voltage drop indicates efficient charge transport within the electrode–electrolyte system [31].

The charge storage kinetics are further analyzed by plotting the logarithm of the peak current versus the logarithm of the scan rate (Fig. 4c). The linear relationship, with a slope (b-value) of approximately 0.98, indicates that the charge storage process is predominantly surface-controlled. The power-law equation ($i = av^b$) is used to examine the relation between peak current and scan rate. This value, which is very close to unity, confirms that the capacitance arises mainly from fast capacitive processes rather than diffusion-limited intercalation mechanisms. The relative contributions of capacitive and diffusion-controlled processes were quantified as shown in Fig. 4d. The results reveal that the capacitive contribution dominates across all scan rates, at 95–100%, further supporting the EDLC-dominated behavior of the material. This suggests that the hierarchical pore structure enables efficient ion adsorption/desorption with negligible diffusion resistance [32].

Electrochemical impedance spectroscopy (EIS) analysis (Fig. 4e) provides further insight into charge-transport properties. The Nyquist plot exhibits a small semicircle in the high-frequency region, corresponding to a low charge-transfer resistance (2.137 Ω), and a nearly vertical line in the low-frequency region, indicative of ideal capacitive behavior. The low intercept on the real axis reflects a small solution resistance (1.055 Ω), confirming good electrical conductivity and effective electrolyte interaction [32].

The variation in specific capacitance with current density is illustrated in Fig. 4f. The AC electrode delivers a high specific capacitance of approximately 191 F/g at 0.25 A/g, which gradually decreases to about 104 F/g at 10 A/g. This decrease is attributed to insufficient time for electrolyte ions to access all active sites at higher current densities. Nevertheless, the electrode maintains reasonable capacitance retention, demonstrating good rate performance and efficient ion transport within the porous carbon framework.

The 3-electrode analysis of lignin-derived hard carbon is further studied electrochemically. The CV curves of the HC electrode (Fig. 5a) exhibit a quasi-rectangular shape over scan rates of 10–80 mV/s, indicating dominant EDLC behavior, with slight deviations attributable to surface redox activity. The retention of curve shape at higher scan rates suggests excellent rate capability and rapid ion transport within the porous carbon framework. Such behavior is typical of disordered porous carbons, in which a high density of accessible surface sites facilitates rapid charge accumulation [33]. HC shows slight distortion in the CV curves, suggesting the presence of diffusion-controlled processes in addition to surface capacitive effects. Furthermore, the current response of AC is significantly higher than that of HC at identical scan rates, reflecting its superior charge-storage capability, which can be attributed to its greater accessible surface area and well-developed porous structure.

The GCD profiles (Fig. 5b) show nearly symmetric triangular shapes, confirming high reversibility and capacitive charge storage at a stable potential window of 0.1 to −1.1 V. The minimal IR drop observed at lower current densities indicates low internal resistance, while the gradual decrease in discharge time at higher current densities reflects limited ion diffusion at fast charging rates. This trend is consistent with porous carbon electrodes, where ion accessibility governs performance at high current densities. However, AC exhibits a much longer discharge time compared to HC at the same current density, confirming its higher specific capacitance. Quantitatively, AC delivers a capacitance of approximately 191 F/g at low current density, whereas HC shows a comparatively lower value of 106 F/g.

The kinetic analysis (Fig. 5c) based on the relationship between peak current and scan rate indicates that both materials predominantly

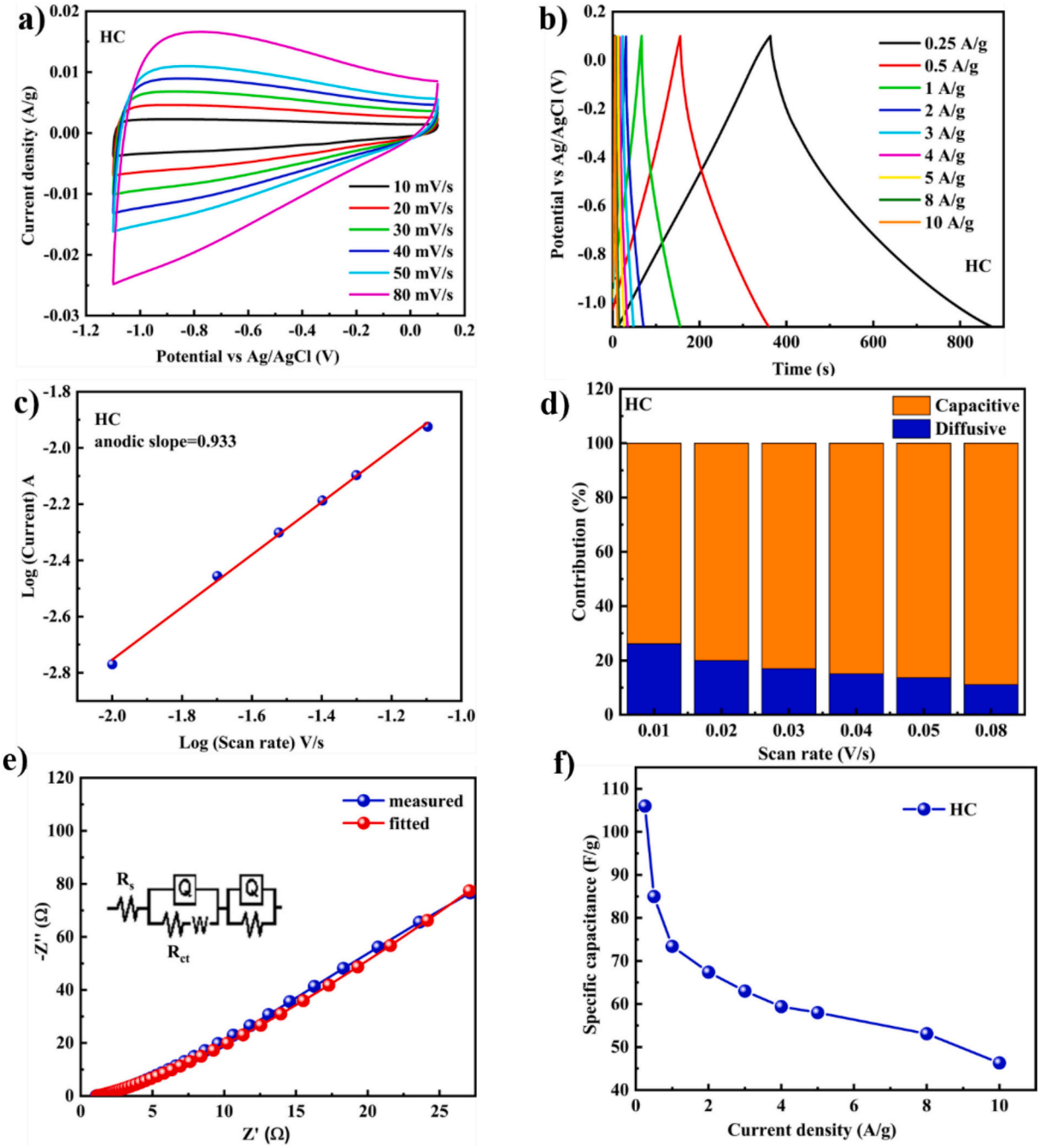

Fig. 5. 3-electrode measurements of lignin derived HC a) CV at varying scan rate in 3 M KOH electrolyte, b) GCD at varying current density, c) power-law analysis of peak current vs scan rate, d) quantitative separation of charge storage contributions at different scan rates, e) Nyquist plot obtained using EIS analysis and equivalent circuit is shown in the inset, and f) specific capacitance vs. current density plot.

exhibit capacitive-controlled charge storage. The calculated b-value at −0.3 V for AC (~0.98) is very close to unity, indicating an almost ideal surface-controlled process. In comparison, HC exhibits a slightly lower b-value (~0.93), suggesting that although capacitive behavior dominates, diffusion-controlled processes make a noticeable contribution. This difference becomes more evident in the quantitative separation of capacitive and diffusion contributions. AC shows 95–100% capacitive contribution across all scan rates, confirming its predominantly EDLC-type charge storage under the tested conditions.

On the other hand, HC exhibits a mixed mechanism, where diffusion contributes significantly at lower scan rates but decreases as the scan rate increases, with capacitive processes becoming dominant at higher scan rates [34]. The quantitative separation of current contributions (Fig. 5d) reveals that at low scan rates, diffusion-controlled processes contribute moderately, whereas at higher scan rates, capacitive contributions dominate (~85–90%). This increasing capacitive dominance at higher scan rates highlights fast surface adsorption/desorption processes, which are essential for high-power applications. Such behavior is commonly observed in porous carbon electrodes with hierarchical pore structures, which facilitate the transport and storage of electrolyte ions.

Unlike highly microporous activated carbon, where ion transport within narrow pores can reduce the apparent b-value, HC facilitates rapid ion adsorption/desorption at readily accessible sites. Additionally, the presence of surface functional groups may introduce fast pseudocapacitive contributions, further enhancing the capacitive response. Such behavior is consistent with previous reports highlighting that ion

transport kinetics and accessibility, rather than surface area alone, govern rate performance in carbon-based electrodes [35–37].

Electrochemical impedance spectroscopy (EIS) provides further insight into the charge-transport properties of the electrodes (Fig. 5e). The Nyquist plots indicate that AC possesses a smaller semicircle in the high-frequency region, corresponding to lower charge transfer resistance (R_{ct}), and a more vertical line in the low-frequency region, indicating ideal capacitive behavior and efficient ion diffusion. In contrast, HC shows a slightly larger semicircle, suggesting higher resistance and comparatively slower charge transfer kinetics. This difference can be attributed to the less accessible pore structure and higher structural disorder in HC. It shows a solution resistance (R_s) of 1.23 Ω and a charge-transfer resistance (R_{ct}) of 4.25 Ω.

The specific capacitance versus current density is depicted in Fig. 5f. The specific capacitance decreases with increasing current density, which is attributed to limited ion diffusion and reduced electrolyte accessibility at higher charge–discharge rates. At low current densities, sufficient time allows effective utilization of the surface, resulting in

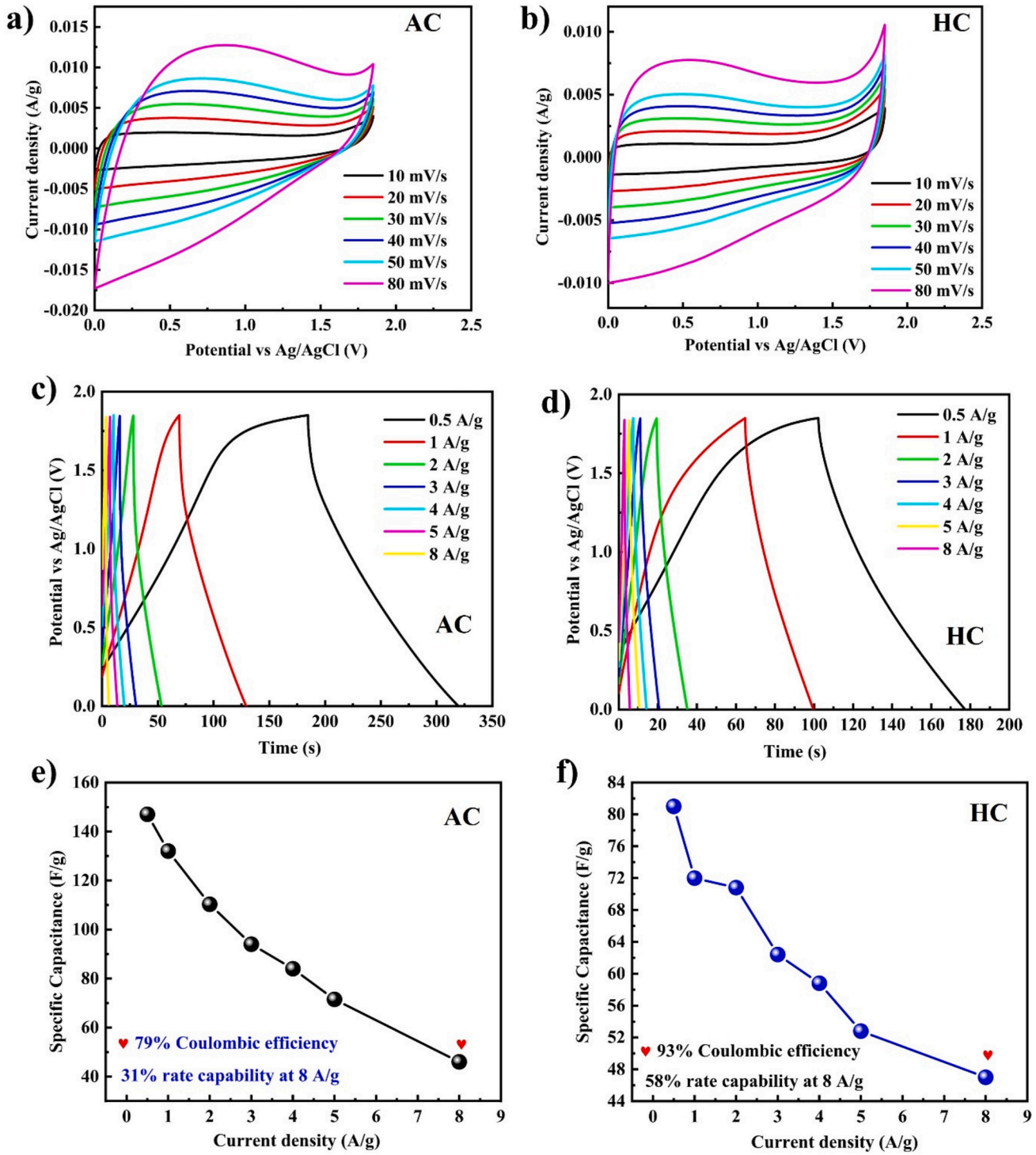

Fig. 6. Electrochemical performance of symmetric supercapacitors based on AC and HC electrodes: a) CV curves of AC//AC, b) CV curves of HC//HC device recorded at different scan rates, c) GCD profiles of AC//AC, d) GCD plot of HC//HC at various current densities, Specific capacitance as a function of current density for e) AC and f) HC symmetric devices.

higher capacitance. Notably, the relatively good capacitance retention at higher current densities indicates favorable rate capability (43% at 10 A/g) and efficient charge transport within the electrode materials.

3.1.2. Symmetric 2-electrode measurements

The electrochemical performance of the fabricated electrodes is further evaluated in a two-electrode symmetric configuration, which provides a more realistic assessment of device-level behavior than three-electrode measurements. In this configuration, both electrodes consist of identical active materials, and the measured capacitance reflects the combined contribution of the two electrodes connected in series. The active mass loading of symmetrical electrodes is the combined mass of the anode and the cathode. It is calculated as 4.59 mg for both symmetrical AC and HC devices.

The cyclic voltammetry (CV) profiles of both AC//AC and HC//HC devices exhibit quasi-rectangular shapes, confirming dominant electric double-layer capacitive behavior (Fig. 6a and b). Notably, the AC-based device shows a significantly larger enclosed CV area than HC, indicating a higher charge storage capacity, consistent with its high specific surface area (1503 $m^2\ g^{-1}$). This suggests that charge storage in AC is primarily governed by extensive ion adsorption within its highly developed microporous network. In contrast, the HC device exhibits a smaller CV area but maintains a more stable shape at higher scan rates, indicating superior rate capability. The slight distortion observed in HC at high scan rates is less severe than in AC, suggesting more efficient ion transport kinetics. This behavior indicates that while AC is optimized for energy storage, HC is better suited for high-power applications due to reduced diffusion resistance and improved ion accessibility [38,39].

The galvanostatic charge–discharge (GCD) curves of both symmetric devices exhibit nearly triangular, symmetric profiles, confirming reversible EDLC behavior (Fig. 6c and d). The AC//AC device exhibits significantly longer discharge times than the HC//HC device, indicating higher specific capacitance and energy storage capacity. However, a noticeable IR drop is observed at the start of discharge, particularly at higher current densities, suggesting increased internal resistance and ion diffusion limitations. In contrast, the HC device exhibits shorter discharge times but relatively smaller distortion at high current densities, indicating better rate performance and lower resistive losses. The improved behavior of HC under high-current conditions further supports its suitability for high-power applications [38].

For a two-electrode symmetric cell, specific capacitance can be calculated based on the total mass of both electrodes: [17].

$$C_{cell} = \frac{I \times \Delta t}{m_{total} \times \Delta V} \tag{2}$$

where I is the current in amperes, Δt is the discharge time in seconds, m_{total} is the total mass of the active material in mg, and ΔV is the potential window.

For a symmetric electrochemical double-layer capacitor (EDLC), the specific capacitance of a single electrode can be derived from the cell capacitance using:

$$C_{se} = \frac{4 \times I \times \Delta t}{m_{total} \times \Delta V} \tag{3}$$

The factor of 4 arises because the two identical electrodes are connected in series, resulting in the total cell capacitance being half that of an individual electrode, while the measured mass corresponds to the combined mass of both electrodes; therefore, a correction factor is required to express the capacitance on a per-electrode basis. The single-electrode specific capacitance is calculated to be 147 F/g and 81 F/g for AC and HC, respectively. The cell-specific capacitance calculated using Eq. (3) is ~37 F/g and ~20 F/g at a current density of 0.5 A/g.

The single-electrode specific capacitance vs. current density is depicted in Fig. 6e and f. AC exhibits poor rate capability, retaining only 31% of its capacitance at 8 A/g due to slow ion diffusion within narrow pores. In contrast, the HC device exhibits lower capacitance (81 F/g) but significantly better rate capability (58% retention). This indicates that HC possesses more accessible surface sites and faster ion transport pathways, minimizing diffusion limitations. As a result, HC demonstrates superior power density, making it more suitable for applications requiring rapid charge–discharge cycles. The HC-based device exhibits a higher coulombic efficiency (93%) than AC (79%), indicating more efficient and reversible charge storage. The lower efficiency in AC can be attributed to ion trapping within ultramicropores and increased resistive losses.

The Nyquist plots of the AC//AC and HC//HC symmetric supercapacitors are shown in Fig. 7a and b, respectively. Both spectra exhibit a typical EDLC response comprising a high-frequency intercept, a non-ideal semicircle in the mid-frequency region, and a slanted line in the low-frequency region. The intercept at the real axis (Z′) in the high-frequency region corresponds to the solution resistance (R_s), which includes the intrinsic resistance of the electrolyte, electrode material, and current collector. The semicircle observed in the mid-frequency region represents the charge transfer resistance (R_{ct}) at the electrode–electrolyte interface. The low-frequency linear region corresponds to the Warburg impedance, associated with ion diffusion within the porous electrode.

The equivalent circuit used for fitting consists of R_s in series with a parallel combination of R_{ct} and a constant phase element (CPE), followed by a Warburg diffusion element. The good agreement between measured and fitted data confirms the validity of the selected model. The AC-based device shows a higher $R_{ct,}$ and the deviation from vertical behavior at low frequencies suggests diffusion limitations, likely due to its highly microporous structure. In contrast, the HC device exhibits a slightly lower R_{ct} but a more vertical low-frequency line, indicating improved ion diffusion and reduced transport resistance [40]. This behavior explains the superior rate capability and power performance observed for HC. The extracted values indicate that R_s is approximately 0.9 Ω (AC) and 1.1 Ω (HC), while R_{ct} is 13.8 Ω (AC) and 2.6 Ω (HC), confirming lower interfacial resistance and better ion-transport characteristics in HC.

The seemingly contradictory observation of higher specific capacitance but larger charge-transfer resistance in AC arises from the fundamental difference between charge-storage and ion-transport mechanisms. While the high surface area and abundant micropores in AC provide a large number of electrochemically active sites, thereby enhancing capacitance, these micropores impose significant diffusion resistance due to ion confinement and desolvation effects. Consequently, this leads to an increase in interfacial resistance (R_{ct}). In contrast, HC, despite its low surface area and reduced capacitance, exhibits a lower R_{ct} due to improved ion accessibility and faster charge-transfer kinetics associated with its relatively open structure [35].

The self-discharge characteristics of the symmetric devices were evaluated by monitoring the open-circuit voltage decay over 10 h, as shown in Fig. 7c. The self-discharge rate was calculated using Eq. (4):

$$SR = \frac{V_0 - V_t}{t} \tag{4}$$

where V_0 is the initial charging voltage, $V_t$is the voltage after time t, and $t$is the self-discharge duration. The AC device exhibits a rapid initial voltage drop followed by a gradual decay, with a self-discharge rate of 0.12 V/h, indicating relatively higher charge redistribution and leakage. This behavior can be attributed to its high surface area and abundant micropores, which facilitate ion rearrangement and provide pathways for internal leakage. In contrast, the HC device exhibits a slower voltage decay, with a lower self-discharge rate of 0.086 V/h, indicating improved charge retention. The reduced self-discharge of HC can be attributed to its relatively compact structure and lower surface reactivity, which suppress charge redistribution and parasitic faradaic reactions.

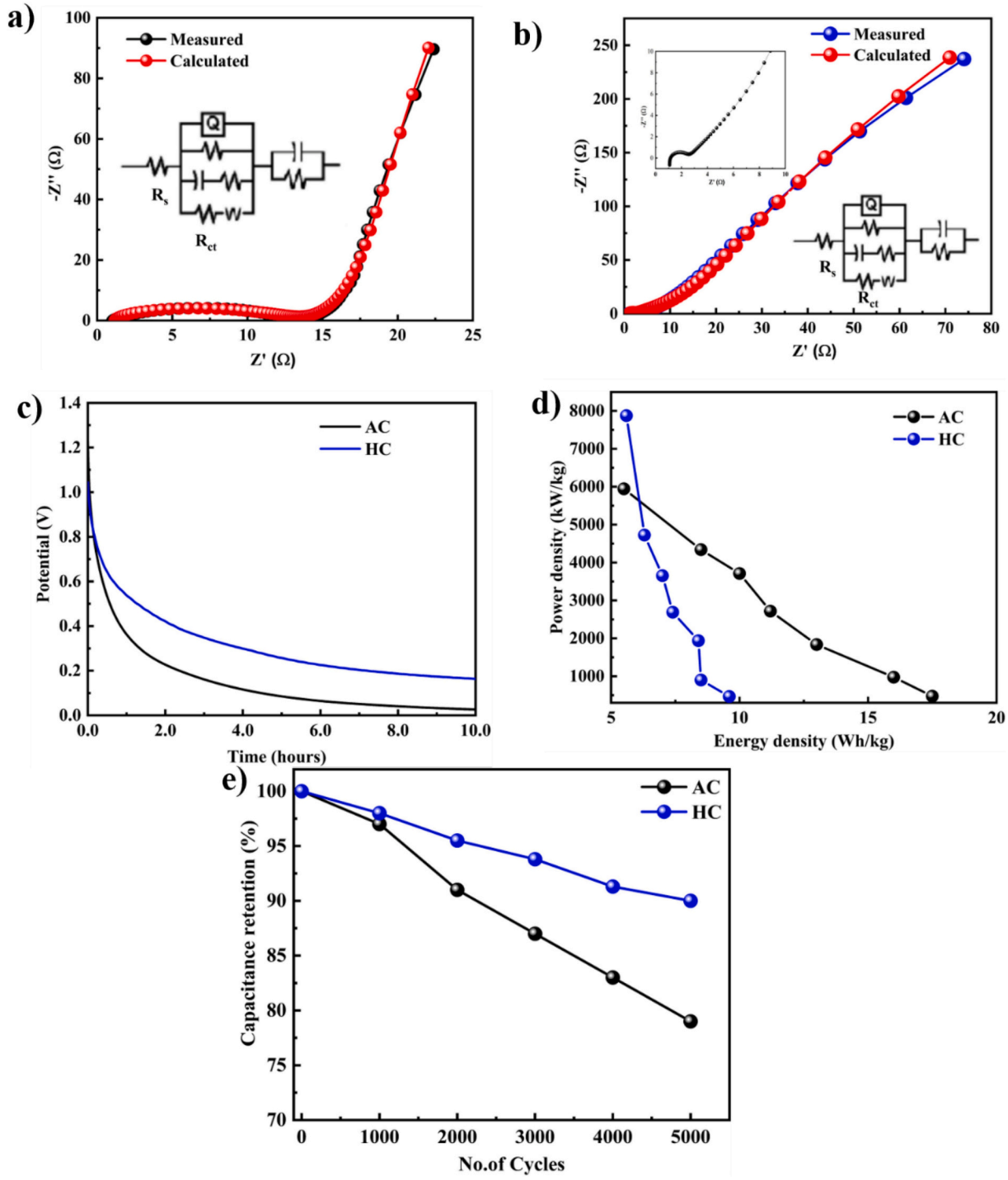

Fig. 7. Nyquist plot for a) symmetric AC device, b) symmetric HC device (equivalent circuits were shown in the inset), c) comparison of self-discharge in AC and HC, d) Ragone plot for as-fabricated symmetric devices, and e) comparison of capacitance retention over 5000 cycles.

The self-discharge behavior in supercapacitors generally follows three mechanisms: (i) ohmic leakage, (ii) charge redistribution within pores, and (iii) parasitic redox reactions. Among these, charge redistribution is dominant in high surface area carbons like AC, leading to faster voltage decay [41].

The Ragone plot shown in Fig. 7d compares the energy density (ED) and power density (PD) of AC- and HC-symmetric devices. The AC-based device exhibits a higher energy density of up to 17.5 Wh/kg, owing to its high specific capacitance, derived from its large surface area. Symmetric AC device delivers a maximum power density of 5.9 kW/kg. In contrast, the HC device delivers lower energy density (9.6 Wh/kg) but significantly higher power density (7.9 kW/kg), particularly at high current densities. This indicates that HC enables faster charge–discharge processes due to improved ion-transport kinetics and reduced diffusion resistance.

The cycling stability of the symmetric devices is evaluated over 5000 charge–discharge cycles, as shown in Fig. 7e. The HC device exhibits better stability, retaining approximately ~90% of its initial capacitance, whereas the AC device shows comparatively lower retention of ~79%. The superior stability of HC can be attributed to its robust structural

framework and reduced ion trapping effects, which minimize structural degradation during repeated cycling. In contrast, the AC device, despite its higher initial capacitance, suffers from gradual performance decay due to pore blockage and ion accumulation within micropores [42].

These results indicate that HC is more suitable for long-term cycling applications, while AC is advantageous for high energy storage. AC exhibits classical electric double-layer capacitance due to its high surface area and hierarchical porosity. In contrast, HC, despite its low surface area, demonstrates capacitive-dominated behavior with minor diffusion contributions, attributed to its dense turbostratic structure and limited ion intercalation under aqueous conditions. This results in enhanced rate capability, higher coulombic efficiency, and suppressed self-discharge in HC-based devices. To combine the advantages of both materials while mitigating their individual limitations, an asymmetric configuration is employed.

3.1.3. Asymmetric 2-electrode configuration

An asymmetric supercapacitor is assembled using activated carbon (AC) as the positive electrode and hard carbon (HC) as the negative electrode, effectively combining high surface-driven capacitance with enhanced conductivity and ion transport. The charge balance between the positive and negative electrodes in the asymmetric supercapacitor was maintained using the relation:

$$\frac{m^+}{m^-} = \frac{C^- \times V^-}{C^+ \times V^+} \tag{5}$$

The superscripts "+" and "−" denote the positive and negative electrodes, respectively. The parameters m, C, and V correspond to the mass, specific capacitance, and operating potential window of each electrode, as obtained from three-electrode measurements. Based on this relationship, the optimized mass ratio of AC to HC was determined to be 1:1.729, ensuring balanced charge storage during operation.

This optimized ratio facilitates efficient utilization of both electrodes, minimizes overpotential, and enhances the overall electrochemical performance and cycling stability of the device. The cyclic voltammetry (CV) curves of the asymmetric AC//HC device at different scan rates are shown in Fig. 8a. The curves exhibit a quasi-rectangular shape with slight distortion at higher scan rates, indicating predominant electric double-layer capacitive behavior with minor resistive contributions. Compared to symmetric devices, the asymmetric configuration enables a similar operating voltage window (1.85 V). The current response increases proportionally with scan rate, suggesting good rate capability and efficient charge propagation. The improved electrochemical behavior arises from the synergistic combination of AC, which provides a high surface area for charge storage, and HC, which facilitates faster ion transport and reduces polarization.

The galvanostatic charge–discharge (GCD) profiles at various current densities are shown in Fig. 8b. The curves exhibit nearly symmetric triangular shapes, confirming the good reversibility and capacitive behavior of the asymmetric device. The extended discharge time at lower current densities indicates enhanced charge storage capability compared to HC alone, while maintaining better rate performance than AC. A relatively small IR drop is observed even at higher current densities, indicating low internal resistance and efficient charge transfer. This improved behavior can be attributed to the complementary roles of AC and HC, with AC contributing to specific capacitance and HC ensuring rapid ion transport, resulting in balanced energy–power performance.

The variation of specific capacitance with current density is shown in Fig. 8c. The asymmetric device delivers a maximum capacitance of 31 F/g at low current density (0.5 A/g) and retains 51.2% of its capacitance at 8 A/g, indicating moderate rate capability. This performance is significantly improved compared to the AC symmetric device, while maintaining higher capacitance than HC. The coulombic efficiency of 95% demonstrates excellent charge-discharge reversibility and minimal energy loss. The improved efficiency compared to AC can be attributed to reduced ion trapping and enhanced ion accessibility due to the presence of HC. Overall, the asymmetric configuration effectively balances capacitance and rate performance.

The Nyquist plot of the asymmetric device is shown in Fig. 8d, along with the fitted equivalent circuit. The spectrum consists of a high-frequency intercept corresponding to the solution resistance (R_s), followed by a small semicircle in the intermediate-frequency region representing the charge transfer resistance (R_{ct}), and a nearly vertical line in the low-frequency region indicating ideal capacitive behavior. The relatively small semicircle diameter suggests low interfacial resistance, confirming efficient charge transfer at the electrode–electrolyte interface. The steep slope in the low-frequency region indicates enhanced ion diffusion and capacitive response. The equivalent circuit fitting, comprising R_s, R_{ct}, constant phase elements (CPE), and diffusion components, shows good agreement with the experimental data. It is calculated that R_s and R_{ct} are 1.04 Ω and 6 Ω, respectively.

Compared with symmetric configurations, the asymmetric device exhibits optimized impedance characteristics by combining the low resistance and fast ion transport of HC. The Ragone plot of the asymmetric AC//HC device is shown in Fig. 8e, illustrating the relationship between energy density and power density. The device delivers a maximum energy density of 14.3 Wh/kg. This ED is much better than symmetric HC and lower than AC. As the energy density increases, the power density gradually decreases. It is observed that the device can deliver a maximum power density of 7.5 kW/kg. This characteristic trade-off between energy and power density is typical of supercapacitor systems. The relatively high energy density is attributed to the high surface area of the AC electrode, while the high power density arises from the fast ion transport and low resistance of the HC electrode. These results confirm that the asymmetric configuration effectively balances energy and power performance.

The self-discharge profile of the asymmetric device is shown in Fig. 8f. A rapid initial voltage drop followed by a slower decay is observed, corresponding to charge redistribution, leakage, and subsequent diffusion-controlled processes. The asymmetric device exhibits a self-discharge rate of 0.089 V/h over 10 h, which is lower than that of the AC//AC device (0.12 V/h). The reduced voltage decay of the AC//HC configuration can be attributed to the relatively stable HC structure, which limits charge redistribution and internal leakage.

The cycling stability of the asymmetric AC//HC device is shown in Fig. 8g, where capacitance retention is plotted as a function of cycle number. The device retains approximately 84% of its initial capacitance after 5000 cycles, indicating good long-term stability. The gradual decrease in capacitance with cycling can be attributed to minor structural degradation and ion accumulation within the electrode pores. However, the relatively high retention compared to AC symmetric devices suggests improved durability due to the incorporation of HC, which enhances structural robustness and reduces internal stress during repeated charge–discharge cycles. These results demonstrate that the asymmetric device not only improves energy–power characteristics but also maintains acceptable cycling stability for practical applications.

To facilitate a clear comparison of the electrochemical performance, the key parameters of the symmetric (AC//AC, HC//HC) and asymmetric (AC//HC) devices are summarized in Table 1.

The superior rate capability, high coulombic efficiency, excellent cycling stability, and suppressed self-discharge observed with the lignin-derived hard carbon electrode are consistent with recent reports on hard-carbon-based supercapacitors. Unlike highly activated carbons, the relatively low surface area and controlled pore structure of hard carbon minimize parasitic reactions and electrolyte decomposition, thereby enhancing efficiency and long-term stability while maintaining rapid ion transport [20,43–45]. To contextualize the performance, a comparison with state-of-the-art lignin-derived carbon electrodes is presented in Table S1, revealing that the present system achieves a superior trade-off between energy density, power density, and cycling durability.

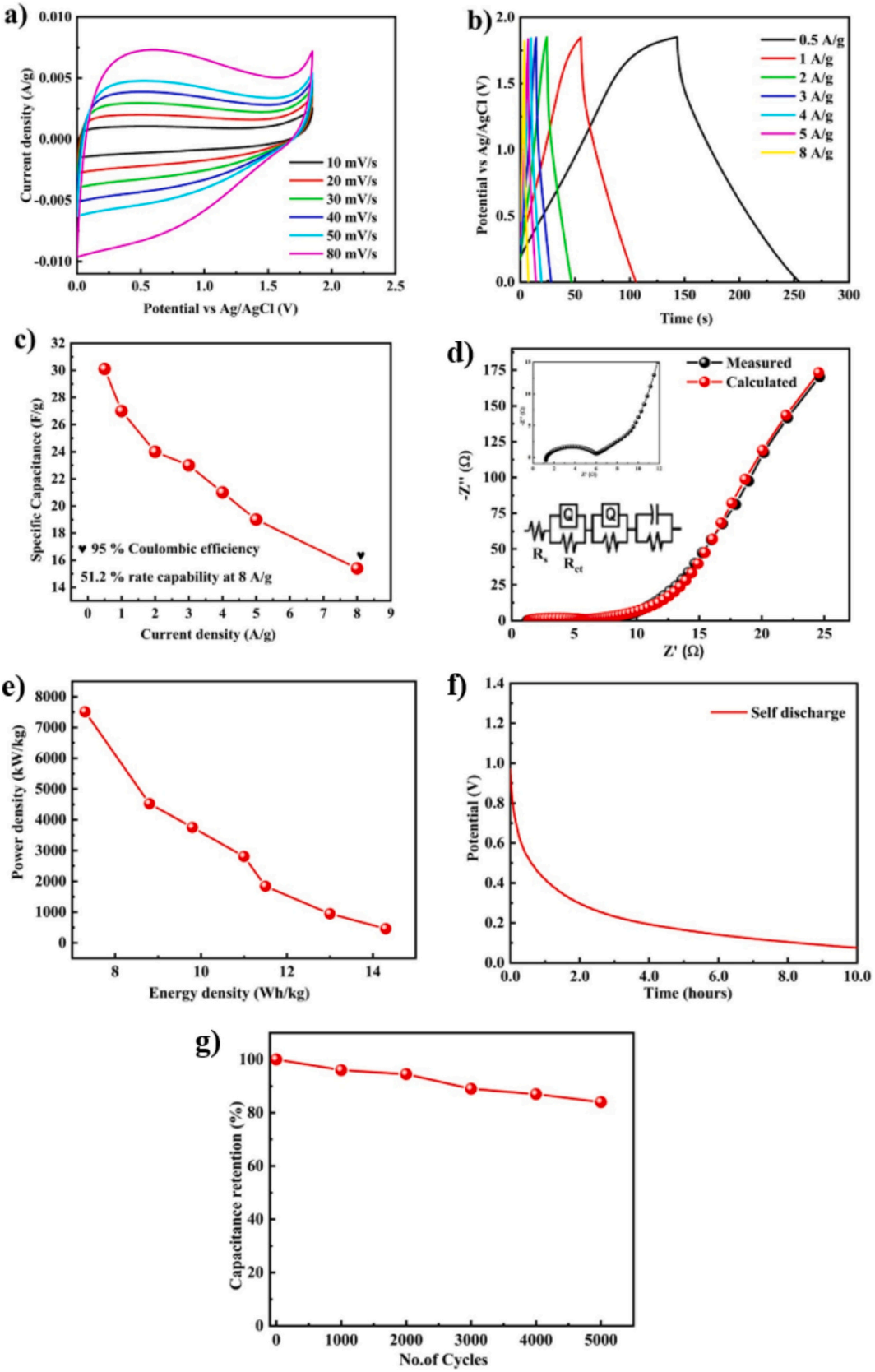

Fig. 8. 2-electrode asymmetric device measurements: a) CV at varying scan rates, b) GCD curves at various current densities, c) specific capacitance vs current density, d) Fitted Nyquist plot with equivalent circuit, e) Ragone plot for an as-fabricated asymmetric device, f) self-discharge plot over 10 h, and g) capacitance retention over 5000 cycles.

Table 1
Comparison of symmetric and asymmetric device performance.

Parameter	AC//AC (symmetric)	HC//HC (symmetric)	AC//HC (asymmetric)
Cell-specific capacitance (F/g) @ 0.5 A/g	37	20	31
Energy density (Wh/kg)	17.5	9.6	14.3
Power density (kW/kg)	5.9	7.9	7.5
Solution resistance, R_s (Ω)	0.9	1.1	1.04
Charge transfer resistance, R_{ct} (Ω)	13.8	2.6	6
Rate capability (%) at 8 A/g	31%	58%	51.2%
Coulombic efficiency (%)	79%	93%	95%
Self-discharge rate (V/h)	0.12	0.086	0.089
Cycling stability (%)/5000 cycles	79%	90%	84%

3.1.4. Post stability analysis

To evaluate the structural and electrochemical robustness of the electrodes, post-cycling analyses were carried out using electrochemical impedance spectroscopy (EIS), scanning electron microscopy (SEM), and X-ray diffraction (XRD).

From the Nyquist plots, clear differences in impedance evolution before and after cycling are observed for both electrodes (Fig.S5). For the AC electrode, the solution resistance (R_s), estimated from the high-frequency intercept, increases from 0.9 Ω (before stability) to 1.04 Ω (after stability). More significantly, the charge transfer resistance (R_{ct}), represented by the semicircle diameter, increases from 13.8 Ω to 21 Ω after cycling (Fig. S5a). Additionally, the low-frequency tail becomes more inclined, indicating increased diffusion resistance and possible pore blockage or reduced electrolyte accessibility. In contrast, the HC electrode exhibits a relatively smaller change in R_s, increasing slightly from 1.1 Ω to 1.14 Ω (Fig. S5b). The R_{ct} also increases but remains comparatively moderate, from 2.6 Ω (before stability) to 4.3 Ω (after stability). Importantly, the Warburg region retains a more linear profile even after cycling, suggesting that ion diffusion pathways remain largely preserved.

Overall, although both electrodes show an increase in impedance after prolonged cycling, the relative change is more pronounced in AC, particularly in terms of diffusion resistance. The HC electrode, despite its higher absolute resistance, demonstrates better retention of ion transport characteristics, reflecting its superior structural stability and consistent electrochemical performance.

The XRD patterns (Fig. S5c) of AC and HC after electrochemical stability testing exhibit a broad diffraction peak centered around ~24–26°, corresponding to the (002) plane of carbon, indicating the predominantly amorphous nature of both materials. Notably, the peak position remains largely unchanged after cycling, confirming that the fundamental carbon framework is well preserved. A slight reduction in intensity and marginal peak broadening are observed, which can be attributed to increased structural disorder or surface modifications induced during repeated charge-discharge processes. In the case of HC, the appearance of minor, irregular features suggests possible electrolyte-induced surface interactions or functional-group rearrangements. Importantly, the absence of any new sharp diffraction peaks indicates that no crystalline degradation products are formed, highlighting the excellent structural stability of both AC and HC electrodes during long-term electrochemical operation.

The morphological evolution of the electrodes was examined using SEM to understand degradation mechanisms at the microstructural level (Fig. S6). Post-cycling SEM images reveal that AC undergoes partial aggregation and restacking, leading to a more compact morphology (Fig. S6a). In contrast, HC maintains a fragmented and porous structure with minimal structural collapse (Fig.S6b). This indicates better morphological stability of HC, supporting its superior electrochemical durability.

The electrochemical degradation is consistent with the evolution of the impedance parameters. After 5000 cycles, the AC//AC device retains 79% of its initial capacitance (21% loss), accompanied by increases in (R_s) from 0.90 to 1.04 Ω (15.6%) and (R_{ct}) from 13.8 to 21 Ω (52.2%). The more inclined low-frequency region further indicates increased diffusion resistance and reduced electrolyte accessibility. In comparison, HC//HC retains 90% capacitance, with only a 3.6% increase in (R_s) (1.10–1.14 Ω), while its low-frequency response remains relatively preserved. The AC//HC device shows intermediate retention of 84%. These results demonstrate that increased interfacial/diffusion resistance and reduced ion accessibility are closely associated with the observed capacitance degradation.

The demonstrated results indicate the potential scalability of black-liquor-derived AC and HC for supercapacitor applications; however, experimental scale-up was not investigated in the present study. Therefore, the scalability claim is considered prospective rather than experimentally validated. Further studies involving larger-scale electrode fabrication and device-level testing are required to establish the practical scalability of the proposed approach.

4. Conclusion

In this work, a sustainable and scalable strategy was demonstrated for the valorization of lignin-rich black liquor into two functionally distinct carbon materials, namely activated carbon (AC) and hard carbon (HC), via a dual-pathway approach involving chemical activation and controlled pyrolysis. The resulting materials exhibit complementary physicochemical and electrochemical properties, enabling their effective utilization in aqueous supercapacitor systems. The AC electrode, with its high specific surface area and hierarchical porosity, delivers superior capacitance and energy density, while the HC electrode, characterized by its dense structure and enhanced electronic conductivity, exhibits remarkable rate capability, high coulombic efficiency, excellent cycling stability, and suppressed self-discharge. Symmetric AC//AC and HC//HC devices confirm the intrinsic advantages of each material, whereas the asymmetric AC//HC configuration successfully integrates their strengths, achieving a balanced energy–power performance. Overall, this study demonstrates a sustainable pathway to convert industrial waste into high-value energy materials, contributing to SDGs 6, 7, 9, and 12 by advancing clean energy, mitigating water pollution, and enabling circular industrial processes.

Despite these advances, a key research gap remains in bridging the trade-off between surface area and electronic conductivity in biomass-derived carbons. In particular, HC exhibits limited capacitance due to its low surface area, restricting its full potential in capacitive energy storage applications. Future work should focus on controlled activation of HC to introduce tailored porosity while preserving its conductive framework, thereby enhancing supercapacitor performance without compromising efficiency and stability. Additionally, deeper insights into charge-storage mechanisms and structure–property relationships will enable the design of next-generation sustainable electrode materials. Overall, this study provides a promising pathway toward high-performance, eco-friendly energy storage systems derived from industrial waste streams.

CRediT authorship contribution statement

Anit Joseph: Writing – original draft, Visualization, Methodology, Investigation, Formal analysis, Conceptualization. **Varna N. Preman:** Writing – original draft, Investigation, Formal analysis, Conceptualization. **Tiju Thomas:** Writing – review & editing, Validation, Supervision, Resources, Project administration, Funding acquisition.

Declaration of Generative AI and AI-assisted technologies in the writing process

The authors used AI-assisted tools (ChatGPT, Perplexity, and Grammarly) solely for language editing and clarity, and take full responsibility for the content of the manuscript.

Declaration of competing interest

The authors declare that they have no known competing financial interests or personal relationships that could have appeared to influence the work reported in this paper.

Acknowledgements

We gratefully acknowledge the Department of Metallurgical and Materials Engineering and the Common Instrument Facility (ICSR) at the Indian Institute of Technology Madras for providing access to characterization facilities. This work is supported by the project SP23241343MMMOEX008673 (SAP22-IITM-057).

Appendix A. Supplementary data

Supplementary data to this article can be found online at https://doi.org/10.1016/j.diamond.2026.114327.

Data availability

Data will be made available on request.

References

[1] K. Thongkam, N. Chaiyut, M. Panapoy, B. Ksapabutr, Biomass-based nitrogen-doped carbon/polyaniline composite as electrode material for supercapacitor devices, Journal of Metals, Materials and Minerals 33 (2023) 1675, https://doi.org/10.55713/jmmm.v33i3.1675.

[2] W. Zhong, W. Su, P. Li, K. Li, W. Wu, B. Jiang, Preparation and research progress of lignin-based supercapacitor electrode materials, Int. J. Biol. Macromol. 259 (2024) 128942, https://doi.org/10.1016/j.ijbiomac.2023.128942.

[3] Y. Han, Z. Li, Y. Long, W. Zhong, C. Zhang, W. Wu, A review on the application of lignin-based carbon materials in supercapacitors: fabrication of multi-dimensional morphologies and heteroatom doping, Int. J. Biol. Macromol. 311 (2025) 144029, https://doi.org/10.1016/j.ijbiomac.2025.144029.

[4] M. Yao, X. Bi, Z. Wang, P. Yu, A. Dufresne, C. Jiang, Recent advances in lignin-based carbon materials and their applications: a review, Int. J. Biol. Macromol. 223 (2022) 980–1014, https://doi.org/10.1016/j.ijbiomac.2022.11.070.

[5] X. Guan, X. Li, X. Zhao, Z. Wang, L. Zhang, J. Ma, Recent advances in hierarchical porous carbon materials derived from lignin in black liquor toward high-performance supercapacitors: a review, J. Energy Storage 111 (2025) 115380, https://doi.org/10.1016/j.est.2025.115380.

[6] K. Jain, M. Singh, K. Yadav, P. Saharan, A. Gupta, S.R. Dhakate, Direct conversion of lignin-rich black liquor to activated carbon for supercapacitor electrodes, Int. J. Biol. Macromol. 270 (2024) 132150, https://doi.org/10.1016/j.ijbiomac.2024.132150.

[7] A. Lu, J. Qin, A review on biomass-derived hard carbon anodes for sodium-ion batteries: from carbon precursors to storage mechanisms, Journal of Metals, Materials and Minerals 36 (2026) e2555, https://doi.org/10.55713/jmmm.v36i1.2555.

[8] A. Ausavasukhi, T. Siriphala, W. Limphirat, S. Nilmoung, Leonardite humic acid activated carbon/MnO_2 composite nanostructures for supercapacitors, Journal of Metals, Materials and Minerals 34 (2024) 1932, https://doi.org/10.55713/jmmm.v34i2.1932.

[9] M.R. Karim, H.J. Park, S.Y. Park, T. Lee, W.H. Nam, J. Choi, J.Y. Cho, W.H. Shin, Low molecular weight lignin derived carbons for sustainable high-performance supercapacitors, J. Energy Storage 103 (2024) 114228, https://doi.org/10.1016/j.est.2024.114228.

[10] V. Kumar, P. Verma, Microbial valorization of Kraft black liquor for production of platform chemicals, biofuels, and value-added products: a critical review, J. Environ. Manag. 366 (2024) 121631, https://doi.org/10.1016/j.jenvman.2024.121631.

[11] G.A. Smook, M.J. Kocurek, Handbook for Pulp & Paper Technologists, Tappi Press, 2016. https://books.google.co.in/books?id=h8YWtAEACAAJ.

[12] R. Rinaldi, R. Jastrzebski, M.T. Clough, J. Ralph, M. Kennema, P.C.A. Bruijnincx, B. M. Weckhuysen, Paving the way for lignin valorisation: recent advances in bioengineering, biorefining and catalysis, Angew. Chem. Int. Ed. 55 (2016) 8164–8215, https://doi.org/10.1002/anie.201510351.

[13] H. Tran, E. Vakkilainen, the Kraft chemical recovery process, 2016.

[14] C.-H. Kim, J.-Y. Lee, S.-H. Park, S.-O. Moon, Global trends and prospects of black liquor as bioenergy, J. Korea Tech. Assoc. Pulp Pap. Ind. 51 (2019) 3–15, https://doi.org/10.7584/JKTAPPI.2019.10.51.5.3.

[15] M.-M. Titirici, R.J. White, N. Brun, V.L. Budarin, D.S. Su, F. del Monte, J.H. Clark, M.J. MacLachlan, Sustainable carbon materials, Chem. Soc. Rev. 44 (2015) 250–290, https://doi.org/10.1039/C4CS00232F.

[16] M. Sevilla, A.B. Fuertes, Sustainable porous carbons with a superior performance for CO_2 capture, Energy Environ. Sci. 4 (2011) 1765–1771, https://doi.org/10.1039/C0EE00784F.

[17] A. Joseph, A. Mathew, T. Thomas, *Trichosanthes cucumerina* derived activated carbon: the potential electrode material for high energy symmetric supercapacitor, ChemNanoMat 10 (2024) e202400112, https://doi.org/10.1002/cnma.202400112.

[18] S. Jha, S. Mehta, Y. Chen, L. Ma, P. Renner, D.Y. Parkinson, H. Liang, Design and synthesis of lignin-based flexible supercapacitors, ACS Sustain. Chem. Eng. 8 (2020) 498–511, https://doi.org/10.1021/acssuschemeng.9b05880.

[19] S. Ghosh, R. Santhosh, S. Jeniffer, V. Raghavan, G. Jacob, K. Nanaji, P. Kollu, S. K. Jeong, A.N. Grace, Natural biomass derived hard carbon and activated carbons as electrochemical supercapacitor electrodes, Sci. Rep. 9 (2019) 16315, https://doi.org/10.1038/s41598-019-52006-x.

[20] H. Chu, Z. Lu, M. Man, S. Song, H. Zhang, J. Cheng, X. Zhao, J. Duan, X. Chen, Y. Zhu, Hard carbon-based electrode boosts the performance of a solid-state symmetric supercapacitor, J. Energy Storage 76 (2024) 109660, https://doi.org/10.1016/j.est.2023.109660.

[21] A.C. Ferrari, J. Robertson, Interpretation of Raman spectra of disordered and amorphous carbon, Phys. Rev. B 61 (2000) 14095–14107, https://doi.org/10.1103/PhysRevB.61.14095.

[22] X.-S. Wu, X.-L. Dong, B.-Y. Wang, J.-L. Xia, W.-C. Li, Revealing the sodium storage behavior of biomass-derived hard carbon by using pure lignin and cellulose as model precursors, Renew. Energy 189 (2022) 630–638, https://doi.org/10.1016/j.renene.2022.03.023.

[23] N. Kitchamsetti, S. Mhin, Advances and prospects of lignin-derived hard carbons for next-generation sodium-ion batteries, Polymers (Basel). 17 (2025), https://doi.org/10.3390/polym17202801.

[24] M. Bermont, C. Davoisne, F. Rabuel, C. Surcin, R. Janot, D. Huo, Revisiting irreversible capacity in lignin-derived hard carbons for sodium-ion batteries: the dominant role of surface functional groups over surface area, J. Power Sources 672 (2026) 239596, https://doi.org/10.1016/j.jpowsour.2026.239596.

[25] W. Li, Y. Zhang, L. Das, Y. Wang, M. Li, N. Wanninayake, Y. Pu, D.Y. Kim, Y.-T. Cheng, A.J. Ragauskas, J. Shi, Linking lignin source with structural and electrochemical properties of lignin-derived carbon materials, RSC Adv. 8 (2018) 38721–38732, https://doi.org/10.1039/C8RA08539K.

[26] S.-Y. Long, Y. Qin, J.-L. Liu, X.-Q. Xian, L.-Q. Zhou, W.-D. Lv, P.-D. Tang, Q.-Y. Wang, Q.-S. Du, Study on the lignin-derived sp2–sp3 hybrid hard carbon materials and the feasibility for industrial production, Sci. Rep. 14 (2024) 5091, https://doi.org/10.1038/s41598-024-54190-x.

[27] W. Luo, C. Bommier, Z. Jian, X. Li, R. Carter, S. Vail, Y. Lu, J.-J. Lee, X. Ji, Low-surface-area hard carbon anode for Na-ion batteries via graphene oxide as a dehydration agent, ACS Appl. Mater. Interfaces 7 (2015) 2626–2631, https://doi.org/10.1021/am507679x.

[28] V. Hoffmann, C. Rodriguez Correa, D. Sautter, E. Maringolo, A. Kruse, Study of the electrical of biobased carbonaceous powder materials under moderate pressure for the application as electrode materials in energy storage technologies, GCB Bioenergy 11 (2019) 230–248, https://doi.org/10.1111/gcbb.12545.

[29] L.L. Zhang, X.S. Zhao, Carbon-based materials as supercapacitor electrodes, Chem. Soc. Rev. 38 (2009) 2520–2531, https://doi.org/10.1039/B813846J.

[30] M. Sevilla, R. Mokaya, Energy storage applications of activated carbons: supercapacitors and hydrogen storage, Energy Environ. Sci. 7 (2014) 1250–1280, https://doi.org/10.1039/C3EE43525C.

[31] P. Simon, Y. Gogotsi, Materials for electrochemical capacitors, Nat. Mater. 7 (2008) 845–854, https://doi.org/10.1038/nmat2297.

[32] S. Sharma, P. Chand, Supercapacitor and electrochemical techniques: a brief review, Results Chem. 5 (2023) 100885, https://doi.org/10.1016/j.rechem.2023.100885.

[33] Y. Ma, C. Ma, J. Wang, X. Gao, Z. Li, Y. Han, Extremely durable supercapacitor enabled by disordered porous carbon with a capacity retention up to 60 000 cycles, J. Mater. Chem. C 13 (2025) 4429–4434, https://doi.org/10.1039/D4TC04734F.

[34] V. Shrivastav, Mansi, P. Dubey, V. Shrivastav, A. Kaur, M. Hołdyński, A. Krawczyńska, U.K. Tiwari, A. Deep, W. Nogala, S. Sundriyal, Diffusion controlled electrochemical analysis of MoS2 and MOF derived metal oxide–carbon hybrids for high performance supercapacitors, Sci. Rep. 13 (2023) 20675, https://doi.org/10.1038/s41598-023-47730-4.

[35] J. Chmiola, G. Yushin, Y. Gogotsi, C. Portet, P. Simon, P.L. Taberna, Anomalous increase in carbon capacitance at pore sizes less than 1 nanometer, Science (1979) 313 (2006) 1760–1763, https://doi.org/10.1126/science.1132195.

[36] B. Dunn, H. Kamath, J.-M. Tarascon, Electrical energy storage for the grid: a battery of choices, Science (1979) 334 (2011) 928–935, https://doi.org/10.1126/science.1212741.

[37] Z. Guo, Z. Xu, F. Xie, J. Jiang, K. Zheng, S. Alabidun, M. Crespo-Ribadeneyra, Y.-S. Hu, H. Au, M.-M. Titirici, Investigating the superior performance of hard carbon anodes in sodium-ion compared with lithium- and potassium-ion batteries, Adv. Mater. 35 (2023) 2304091, https://doi.org/10.1002/adma.202304091.

[38] Y. Zhang, X. Li, Z. Li, F. Yang, Evaluation of electrochemical performance of supercapacitors from equivalent circuits through cyclic voltammetry and

galvanostatic charge/discharge, J. Energy Storage 86 (2024) 111122, https://doi.org/10.1016/j.est.2024.111122.
[39] S. Rudra, H.W. Seo, S. Sarker, D.M. Kim, Supercapatteries as hybrid electrochemical energy storage devices: current status and future prospects, Molecules 29 (2024), https://doi.org/10.3390/molecules29010243.
[40] C.T. Hung, P.T. Williams, Applications of impedance spectroscopy. In Impedance Spectroscopy (eds E. Barsoukov and J.R. Macdonald), (n.d.) 258–273. doi:https://doi.org/10.1002/9781119381860.ch4.
[41] B.E. Conway, Electrochemical behavior at porous electrodes; applications to capacitors, in: Electrochemical Supercapacitors: Scientific Fundamentals and Technological Applications, Springer US, Boston, MA, 1999, pp. 377–416, https://doi.org/10.1007/978-1-4757-3058-6_14.
[42] F. Béguin, V. Presser, A. Balducci, E. Frackowiak, Carbons and electrolytes for advanced supercapacitors, Adv. Mater. 26 (2014) 2219–2251,2283, https://doi.org/10.1002/adma.201304137.
[43] J. Ni, Y. Huang, L. Gao, A high-performance hard carbon for Li-ion batteries and supercapacitors application, J. Power Sources 223 (2013) 306–311, https://doi.org/10.1016/j.jpowsour.2012.09.047.
[44] H. Zhang, M. Zhu, J. Zhou, Hard-soft carbon with tailored graphitization for high performance supercapacitors, J. Energy Storage 66 (2023) 107406, https://doi.org/10.1016/j.est.2023.107406.
[45] M. Gowtham, V. Gayathri, N.P. Pratheeb, D. Prabha, M. Elango, X. Lin, S. Sangaraju, Progress and challenges in carbon nanomaterial-based supercapacitors: towards sustainable high-energy storage, Renew. Sust. Energ. Rev. 235 (2026) 116930, https://doi.org/10.1016/j.rser.2026.116930.